AGU PUBLICATIONS

JGR

Journal of Geophysical Research: Space Physics

RESEARCH ARTICLE

10.1002/2014JA019887

Key Points:
- Total energy input during a flare determines the magnitude of TEC perturbation
- TEC perturbation lasted >12 h at the local noon of the time of the flare
- The TEC perturbation due to a flare is sensitive to the background state

Correspondence to:
J. Zhu,
zhjie@umich.edu

Citation:
Zhu, J., and A. J. Ridley (2014), The effect of background conditions on the ionospheric response to solar flares, *J. Geophys. Res. Space Physics*, *119*, 5060–5075, doi:10.1002/2014JA019887.

Received 12 FEB 2014
Accepted 29 MAY 2014
Accepted article online 6 JUN 2014
Published online 18 JUN 2014

The effect of background conditions on the ionospheric response to solar flares

Jie Zhu[1] and Aaron J. Ridley[1]

[1]Department of Atmospheric, Oceanic and Space Sciences, University of Michigan, Ann Arbor, Michigan, USA

Abstract The ionospheric response to two X5 solar flares that occurred in different seasons was investigated using the global ionosphere-thermosphere model. Two questions were investigated: (a) how do different solar flares with similar X-ray peak intensities disturb the ionosphere during the same background and driving conditions? and (b) how do the geomagnetic field and season affect the ionospheric response to solar flares? These questions were investigated by exchanging the two X5 flares for each other so that there were two pairs of flares with (1) the same background conditions but different irradiances and (2) different background conditions but the same irradiance. The simulations showed that the different solar flares into the same background caused ionospheric disturbances of similar profiles but different magnitudes due to differences in the incident energies, while the same flare spectra caused perturbations of similar magnitudes but different profiles in different backgrounds. On the dayside, the response is primarily controlled by the total integrated energy of the flare, independent of the background. For the northern and southern polar regions, the response is strongly controlled by the solar zenith angle and the incident energy, while the background plays a secondary role. On the nightside, the background conditions, including the magnetic field and season, play a primary role, with the neutral winds and electrodynamics driving the ionospheric response.

1. Introduction

Interest in the influence of large solar flares on the Earth's ionosphere has gradually increased over the last few decades due to its deleterious effect on radio wave communication and navigation [*Garriott et al.*, 1967; *Davides*, 1990]. Enhanced X-ray and extreme ultraviolet (EUV) irradiance during a solar flare causes increased ionization in the lower ionosphere (*D* and *E* regions) all the way up to the *F* region, depending on the flare spectrum. The increase of electron density in the *F* region is responsible for the increased total electron content (TEC) [*Mendillo et al.*, 1974]. This phenomenon, known as a "sudden ionospheric disturbance," has been extensively studied for several decades [*Donnelly*, 1967; *Jones*, 1971; *Stonehocker*, 1970]. Measurements from the ground-based worldwide Global Positioning System (GPS) network have recently been used to map TEC globally [*Coster and Komjathy*, 2008; *Rideout and Coster*, 2006]. The sudden increase of TEC has been found to be linearly related to the cosine of the solar zenith angle (SZA) [*Zhang and Xiao*, 2003, 2005]. It was also found that both the flare-induced TEC variation rate, which was derived by differencing the vertical TEC measured by a station-satellite pair at continuous epochs, was proportional to the increase in irradiance caused by the flare and inversely proportional to the Chapman function [*Wan et al.*, 2005]. Based on the GPS measurements, an ionospheric solar flare activity indicator was given by the solar zenith angle and the TEC variation rate [*Xiong et al.*, 2013]. The solar EUV flux, instead of the X-ray flux, was found to be primarily responsible for the increased TEC during and immediately after solar flares [*Tsurutani et al.*, 2009]. The X17 flare on 28 October 2003 increased the total electron content of the subsolar ionosphere by up to 30% in about 5 min [*Tsurutani et al.*, 2005]. By using the effect of partial shadowing of the atmosphere by the Earth, the contribution from different ionospheric regions to the TEC enhancements caused by the 14 July 2000 solar flare was estimated by *Leonovich et al.* [2002]. They found that about 20% of the TEC increase correspond to the ionospheric region lying below 100 km, about 5% of the increase came from the *E* region (100–140 km), about 30% came from the F_1 layer (140–200 km), and about 30% from the region above 300 km [*Leonovich et al.*, 2002]. *Xiong et al.* [2011] found that the electron density in the *E* region was greater than that in the *F* region during the limb solar flare on 7 September 2005, which was mainly attributed to weak enhancements in the EUV flux and strong enhancements in the X-ray flux during this flare.

Despite the fact that GPS measurements have provided an effective way of detecting slant TEC disturbances due to solar flares, it still is difficult to observe the global ionospheric disturbance in detail, due to large gaps in the GPS station coverage around the globe. With the development of global models of the upper atmosphere using high-resolution solar spectra, the ionospheric response to dynamic solar forcing can be investigated more completely than before. Models also provide ways to probe the effects of individual driving forces, which is difficult to do with nature. The National Center for Atmospheric Research thermosphere-ionosphere-mesosphere electrodynamics general circulation model has been used to investigate how the location of a solar flare on the solar disk affects the thermospheric and ionospheric response. *Qian et al.* [2010] showed that flare-driven changes in the *F* region, total electron content (TEC), and neutral density in the upper thermosphere are 2–3 times stronger for a disk-center flare than a limb flare, due to the importance of the EUV enhancement. These model results are in agreement with the experimental results presented by *Leonovich et al.* [2010]. It was also found that solar flares can impact the ionospheric electrodynamics by weakening the upward E × B drift in the magnetic equatorial region during solar flares. This results in a decreased height and a reduced electron density of the F_2 peak [*Qian et al.*, 2012]. Significant and long-lasting perturbations in TEC on the nightside have been shown in simulations by the global ionosphere-thermosphere model (GITM) [*Ridley et al.*, 2006] due to dynamical changes in the neutral atmosphere [*Pawlowski and Ridley*, 2009].

The study presented here explored how the background geomagnetic and season affects the ionospheric response to different solar flares with similar flare classes by using a global ionosphere-thermosphere model. Specifically, two questions were examined: (a) What causes the ionosphere to react differently to different flares that have similar peak magnitudes? and (b) How different would the ionospheric response be to the same flare if the flare took place in a different season or with a different magnetic field configuration?

2. Model

To address these questions, the global ionosphere-thermosphere model (GITM) was used. GITM is a three-dimensional, spherical coordinate model that uses an altitude-based grid [*Ridley et al.*, 2006]. The model solves the continuity, momentum, and energy equations in the thermosphere and ionosphere with the realistic sources terms. The ion flow velocities are assumed to be in steady state, allowing the momentum equation to be solved by taking the gradient in pressure, gravity, neutral winds, and electric fields into account. GITM incorporates multiple physical drivers, including high-latitude electric fields, auroral particle precipitation, solar EUV inputs, and tides. In this case, the *Weimer* [2005] model was used to specify the high-latitude electric field; a statistical model of electron precipitation based on hemispheric power was used to specify the aurora [*Fuller-Rowell and Evans*, 1987], and an empirical model of the thermosphere was used to specify the tidal structure of the neutral atmosphere just below 100 km altitude [*Hedin*, 1987]. The equatorial electrodynamics were solved for in a self-consistent way by using the technique described by *Richmond* [1995]. For all simulations described below, unless otherwise specified, the International Geomagnetic Reference Field (IGRF) was used to describe the magnetic topology. The solar irradiance spectrum calculated by the Flare Irradiance Spectral Model (FISM) [*Chamberlin et al.*, 2007] was used to drive the model. FISM is an empirical model that estimates the solar irradiance at wavelengths from 0.1 nm to 190 nm at 1 nm resolution with a time cadence of 60 s, which is fast enough to capture solar flares [*Chamberlin et al.*, 2007]. FISM uses the Geostationary Operational Environmental Satellite X-Ray Sensor 0.1–0.8 nm channel, Thermosphere Ionosphere Mesosphere Energetics and Dynamics Solar EUV Experiment, Solar Stellar Irradiance Comparison Experiment, and $F_{10.7}$ as inputs to calculate the solar irradiances.

3. Methodology

This study explores the response of the ionosphere to two X5 flares. It was speculated that the response may depend on both the flare spectrum and the thermospheric and ionospheric background conditions when the flare occurred. In order to explore these dependences, multiple simulations of the coupled system were conducted. Each simulation was carried out using different conditions in order to determine the role of that particular condition on the ionospheric response to a solar flare.

The two flares that were explored were those on 14 July 2000 and 6 April 2001. These two flares had almost identical classes: X5.7 and X5.6 respectively. Solar flares are classified according to the peak brightness in the

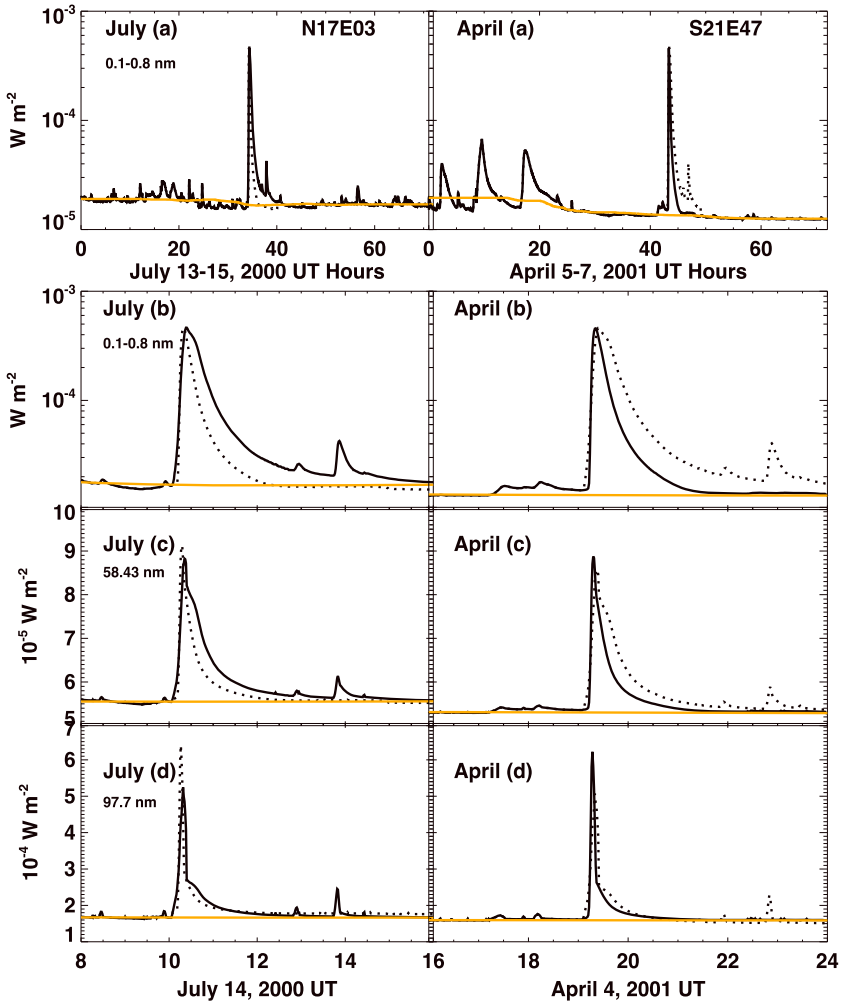

Figure 1. (a) Solar irradiances at 0.1–0.8 nm wavelength of the real flare (solid line) and the imaginary flare superposed on the real flare time (dashed line) for 3 days; (b–d) flare irradiances at 0.1–0.8 nm, 58.43 nm, and 97.7 nm for 8 h. The left and right columns show the July and April flares respectively. The yellow lines represent the 12 h medianed solar irridiances at corresponding wavelengths.

0.1 nm to 0.8 nm X-ray wavelength range. This means that the two flare should have nearly identical peak intensities in X-ray wavelengths but could have different brightnesses in EUV wavelengths.

Figure 1 shows the irradiances at different wavelengths for the flares in July (left) and April (right). Row 1 (a) shows the 0.1–0.8 nm X-ray irradiance for 3 days to provide a long-term context to the flares. Rows 2–4 show the irradiances in 0.1–0.8 nm (b), 58.43 nm (c), and 97.7 nm (d) surrounding the flares. The yellow lines show the 12 h medianed irradiances at corresponding wavelengths. The two EUV wavelengths, 58.43 nm and 97.7 nm, were plotted because of the large cross section of atomic oxygen at 58.43 nm and of molecular oxygen and molecular nitrogen near 97.7 nm (972.5 nm) [*Huffman*, 1969]. The irradiances in 0.1–0.8 nm increased by a factor of approximately 40 and showed identical peaks for the two flares. The July flare lasted approximately twice as long above 10^4 W/m^2 than the April flare. The irradiance at 58.43 nm increased by almost a factor of 2 for both flares. The April flare peaked slightly higher but with a shorter duration than the July flare. At 97.7 nm, the duration of the two flares were similar, and the peak of the April flare was approximately one third higher than the July flare. The duration of the flare decreased with increasing wavelengths.

The July flare took place in Sunspot Region 9077, 17°N 03°E, which was near the center of the solar disk when the flare occurred. The April flare was in Region 9415, 21°S 47°E, which was more toward to the solar limb [*SpaceWeatherLive*, 2014]. The spectra of the two flares when the wavelength of 97.7 nm peaked

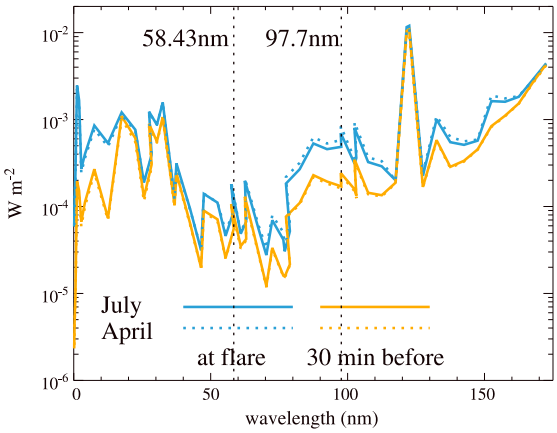

Figure 2. Spectrum of solar irradiances when the wavelength 97.7 nm reached peak (1021 UT and 1918 UT for the July and April flares respectively). The blue lines show the spectrum at the peak; the yellow lines show the spectrum 30 min before. The solid lines indicate the July flare; the dashed lines indicate the April flare. The two black dashed lines mark the two wavelengths, 58.43 nm and 97.7 nm.

(i.e., 1021 UT and 1918 UT for the July flare and the April flare, respectively) are shown in Figure 2. The blue solid and dashed lines show the spectra for the July flare and the April flare respectively when the flux at a wavelength of 97.7 nm reached its peak intensity. The orange solid and dashed lines show the spectra 30 min before for the July and April flares, respectively. Both of the flares produced similar enhancements in the X-ray wavelengths (~0.1 to ~25 nm) and the EUV wavelengths from ~80 to ~120 nm, which was different than the flare studied by *Qian et al.* [2010], which was an X17 flare. It was known that center-to-limb variations of active regions exist in observation of the solar disk as the Sun rotates [*Worden et al.*, 2010]. Contrary to the expectation that the EUV irradiance of a limb flare would be lower than a center flare with identical flare classes, the April flare produced slightly higher EUV irradiance. This was possibly because the April flare produced significantly more EUV irradiance in the flare region so that even after the absorption by the solar atmosphere due to the center-to-limb effect, the EUV emissions still were higher than the center July flare.

In order to explore the difference in the ionospheric response between two solar flares with nearly identical classes, the spectrum of the July flare was grafted to the period when the April flare occurred and termed the imaginary April flare. The grafted time period was 5 h, starting at the flare onset. The same process was done to the April flare to make an imaginary July flare. By moving the flares, it was expected that the ionospheric differences caused by the different flare spectra could be isolated and evaluated. The "imaginary" flares are indicated as dashed lines in Figure 1.

The real July X5.7 flare lasted for ~40 min (1003 UT–1043 UT) [*Space Weather Prediction Center* (*SWPC*), 2013]. The main flare was followed by a small flare (M3.7) that occurred from 1344 UT to 1400 UT [*SWPC*, 2013], about 4 h later than the main flare. This small flare was also grafted to the April time period as it occurred within 5 h of the main onset. The real X5.6 April flare lasted for only ~21 min (1920 UT–1931 UT) [*SWPC*, 2013]. Three small flares (an M3.1 from 0200 UT to 0311 UT, an M8.4 from 0837 UT to 0954 UT, and an M5.1 from 1657 UT to 1814 UT respectively) occurred 1 day before the main flare [*SWPC*, 2013]. Since they were before the main flare, these small flares were not grafted to the July time period.

Taking the energy of the solar irradiance during the flare by integrating the irradiances in all wavelengths from 0.1 nm to 175 nm for an hour starting immediately after the solar flare onset, and using the time preceding the flare as a baseline, the real July flare increased the solar irradiance energy by 15.8%, while the real April flare increased the total energy by 11.3%. The ratio between the extra energy in the real July flare and the real April flare was 1.4. This shows that two flares, of the almost identical peak intensity, may differ significantly in total energy. X-rays and EUV are the primary sources of ionization in the *E* and *F* regions respectively [*Qian et al.*, 2010; *Leonovich et al.*, 2010]; therefore, EUV is expected to be a more important source of TEC enhancements, and the energy ratio in EUV wavelengths was expected to be more relevant to the ratio of the TEC enhancements caused by the two flares. Comparing the flare energy by integrating the irradiances in EUV wavelengths from 25 nm to 120 nm shows that the real July flare increased energy by 10.98% and the real April flare increased by 7.79%. The ratio between the extra EUV energy in the real July flare and the real April flare was 1.3. This indicates that the differences between the two flares in the total integrated irradiances in X-ray wavelengths were greater than the total integrated irradiances in the EUV wavelengths.

Each flare event was simulated twice, once with the flare, using FISM data and once without the flare, using a running 12 h box-medianed FISM data. The simulations used the solar wind and interplanetary magnetic field data measured by the Advanced Composition Explorer (ACE) and delayed for an appropriate amount

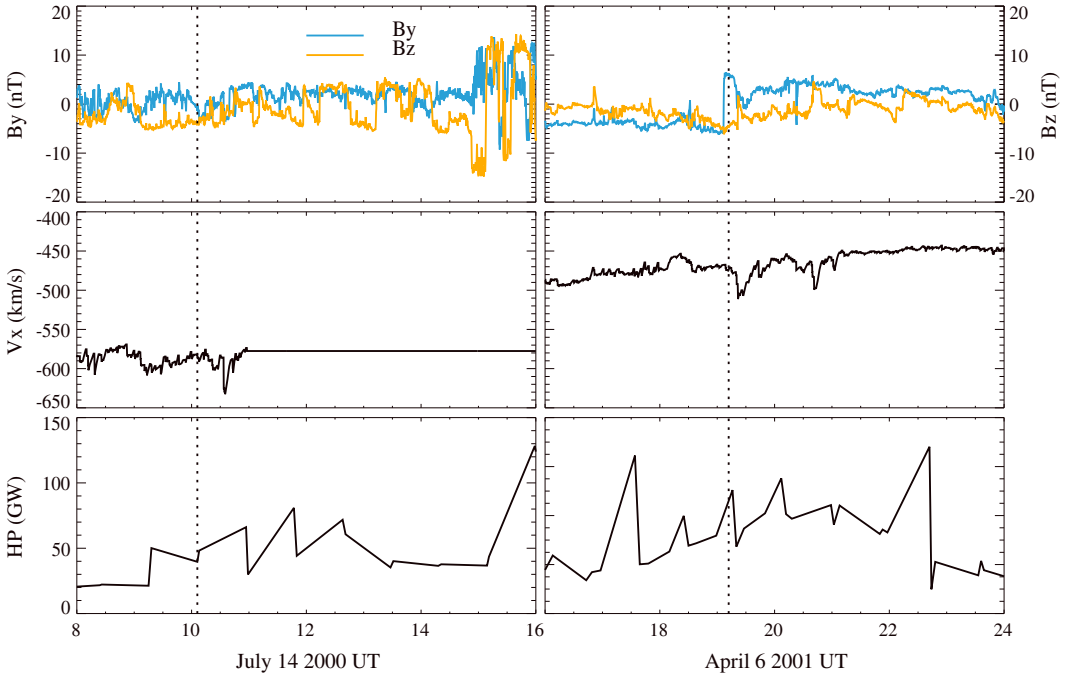

Figure 3. (top row) The interplanetary magnetic field, B_y (blue) and B_z (yellow), (middle row) solar wind speed, and the (bottom row) Northern Hemispheric power during the July flare (left) and April flare (right). The vertical lines show the onset of the flares.

of time and the hemispheric power measured by the National Oceanic and Atmospheric Administration (NOAA) satellites, as shown in Figure 3. The solar wind velocity V_x was unavailable after the July flare onset, so it was replaced with fixed values. All of the external drivers (i.e., IMF and hemispheric power...) except the solar irradiance were the same in the background and flare simulations. The difference between the simulations with and without the flare quantified the ionospheric response to only the solar flare, excluding perturbations due to the other drivers. The perturbation (in percentage) was defined as

$$\text{Perturbation} = 100\% \times \frac{\text{Value}_w - \text{Value}_{wo}}{\text{Value}_{wo}},$$

where Value_w and Value_{wo} were the simulated quantity of interest with the FISM spectrum and with the smoothed FISM spectrum respectively. Four regions of the ionosphere were explored to determine the difference between direct and indirect effects of the solar flares: (a) dayside (solar zenith angle or SZA $< 30°$); (b) nightside (SZA $> 150°$); (c) north polar region (or N.P.: latitudes $> 45°$); and (d) south polar region (or S.P.: latitudes $< -45°$).

4. Results

4.1. TEC Perturbation

Figure 4 shows the regionally averaged TEC perturbation on 14–15 July 2000. The real and imaginary July flares show similar perturbation profiles. The ratios between the real and imaginary peak ionospheric perturbations were 1.42 on the dayside, 1.37 on the nightside, 1.37 in the north polar, and 1.33 in the south polar regions. The dayside ratio was close to the ratio of the total integrated flare energy between the real and imaginary flares (1.40), and the ratios on the nightside, the north polar region and the south polar region, were between the ratios of the total integrated flare energy and of the EUV integrated energy (1.30). As the TEC was decreasing from its most perturbed state, there was a small secondary intensification around 3 h after the initial increase, most noticeable on the dayside for both the real and imaginary flares and the north polar region for the real flare. For the real July flare, this was most likely due to the second intensification in the solar EUV which occurred at this time. For the imaginary flare, a small perturbation on the dayside still occurred, which implied that dynamics played a role in creating this secondary peak.

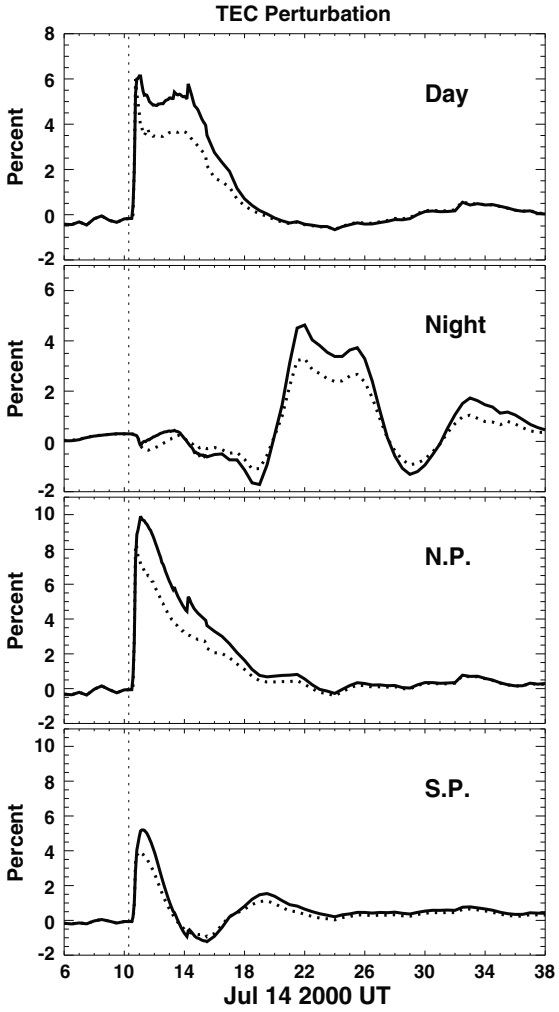

Figure 4. Regionally averaged TEC perturbation on 14–15 July 2000 (dayside: solar zenith angle (SZA) < 30°; nightside: SZA > 150°; north polar region (N.P.): latitudes > 45°; and south polar region (S.P.): latitudes < −45°). The flares began around 1003 UT (indicated as the vertical lines on each panel). The solid line and the dashed line are for the real and the imaginary flares respectively.

The nightside TEC perturbation started ~12 h later than the perturbations in the other regions. This is because the TEC perturbation did not propagate with the sound speed as the neutral perturbation does [*Pawlowski and Ridley*, 2008]. Instead, the flare caused a vertical shift of the ionosphere near the subsolar point, which remained in the same longitudinal sector until recombination caused the perturbation to decay. The nightside only registered an increase when the longitude sector that was near the subsolar point at the time of the flare rotated into this region. The TEC perturbation in this longitude sector was able to last longer than 12 h, but less than 24 h, as indicated by the lack of increase in TEC on the dayside 24 h later. As the North Pole was directed more toward to the Sun, being the summer hemisphere, the TEC perturbation in the north polar region was larger than that in the south polar region. The dayside was expected to have the greatest perturbation of all the regions; however, that was not the case. The reason the percentage change in the north polar region was ~3% higher than on the dayside was that the background TEC on the dayside was greater than that in the north polar region, so the larger real perturbation on the dayside was a smaller percentage change than what occurred in the Northern Hemisphere.

Figure 5 shows the regionally averaged TEC perturbation on 6–7 April 2001. The real and the imaginary flares once again caused very similar profiles of TEC perturbation. However, the perturbation caused by the imaginary flare was larger than the perturbation caused by the real flare since the imaginary flare contained more energy. As the flare occurred near equinox, the north polar and the south polar regions received similar amounts of flare radiance, and they therefore responded with similar perturbation amplitudes. The secondary flare of the imaginary April flare caused a slight increase in the perturbation on the dayside, north polar and south polar regions; however, these responses were not as sharp as those in Figure 4. This indicates that there was something different that occurred during the time periods, even though the flare spectra of the real July flare and the imaginary April flare were identical. The nightside perturbation in response to the main flare was roughly 12 h later than the response in the other three regions. This is once again because of the lack of propagation in the ionospheric response and the persistence of the perturbation for the 12 h it took to rotate to the nightside.

The background middle and low-latitude distribution of TEC at different times before, during, and after the July flare is shown in Figure 6. Additionally, the TEC difference distributions between the real (middle) and imaginary (bottom) flares and the background simulations are shown. The dark diamond (triangle) indicates where noon (midnight) was located at the time of the plot, while the light diamond indicates the subsolar location at the time of the flare. The black line near the 0° latitude marks the geomagnetic equator. The TEC distribution of the nonflare simulation shows two bands of high TEC existing along the geomagnetic equator due to the equatorial dynamo effect. A dayside eastward electric field along with the north

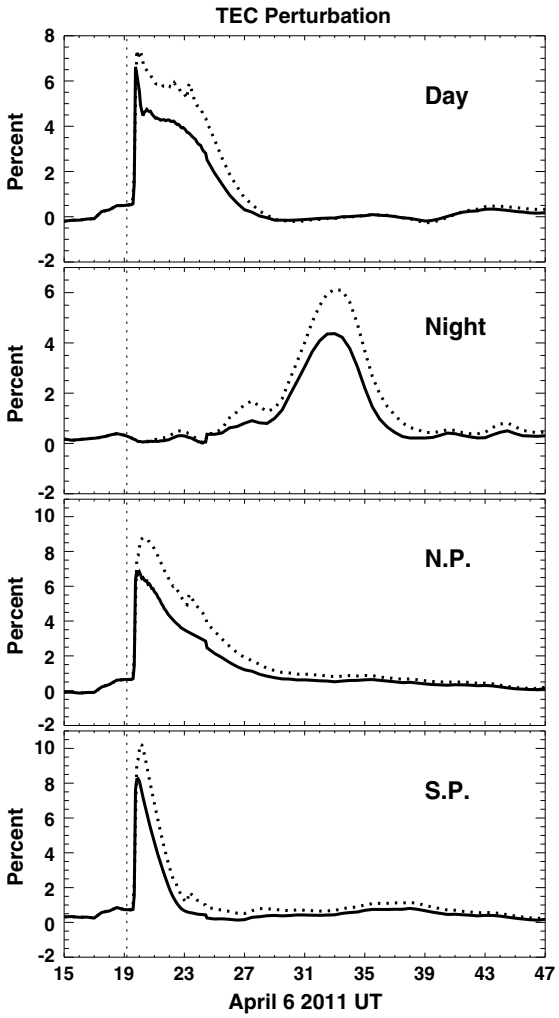

Figure 5. Regionally averaged TEC perturbation on 6–7 April 2001. Regions were defined the same as that in Figure 4. The flares began around 1910 UT (indicated as the vertical lines on each panel). The solid line and the dashed line are for the real and the imaginary flares respectively.

component of the geomagnetic field causes ions to drift upward. Forced by gravity and gradients in pressure, ions flow down field lines away from the magnetic equator on both sides, resulting in two bands of high TEC along the geomagnetic equator. For the TEC difference, the figures at 1000 UT show the background ionosphere before the flares occurred, which were the same for the real and imaginary flares. This is not zero everywhere because the nonflare simulation was a median filter of the FISM inputs, which means that there were small differences in the EUV drivers between the runs even in nonflare time periods. At 1100 UT, there was an increase in TEC across the entire dayside as seen in the difference plots. At 1500 UT, the perturbed region was mostly confined to just off the magnetic equator, with some perturbations on the nightside in the Northern Hemisphere. The largest perturbations at 1500 UT were just a bit west of the location of the subsolar point at the time of the flare. From 1500 UT to 2500 UT (i.e., 0100 UT on 15 July 2000), the distribution of the TEC perturbation remained roughly the same but decayed gradually. The region of increased TEC near the longitudinal sector of the subsolar point at the time that the flare occurred lasted longer than 12 h, such that when it rotated onto the nightside (midnight is indicated by the triangle), a perturbation was registered in this region. The distribution of the TEC perturbations caused by the real and imaginary July flares was very similar. The perturbation was greater in the summer hemisphere (the Northern Hemisphere) than the winter hemisphere (the Southern Hemisphere). The TEC perturbations decayed with a similar structure near the geomagnetic equator. However, the perturbation caused by the real July solar flare was stronger than that caused by the imaginary flare. This was because the real July flare contained more energy than the imaginary flare.

Figure 7 shows the low and middle latitude distribution of the background TEC and the TEC difference before and after the flare on 6–7 April in the same format as Figure 6. The first column, 1900 UT, shows the TEC and difference just before the flare. As shown in Figure 6, the nonflare simulation shows two bands of high TEC existed just off the geomagnetic equator due to the equatorial dynamo effect. At 2000 UT, the difference plots (middle and bottom) showed that TEC was perturbed across the dayside as seen in the difference plots. At 2400 UT, the perturbation was more concentrated around the geomagnetic equator. At 2900 UT (i.e., 0500 UT on 7 April 2001), the perturbation area remained in the same longitude sector that had rotated to the nightside. Simultaneously, a hole occurred right at the magnetic equator surrounded by areas of increased TEC, which may have resulted from the equatorial dynamo. At 3400 UT (i.e., 1000 UT on 7 April 2001), the perturbation still existed but was reduced compared to the previous time.

The distributions of the TEC perturbations caused by the real and the imaginary April flares were quite similar to each other. Since the imaginary April flare contained more energy, the perturbation caused by this flare was stronger than the perturbation caused by the real flare. The perturbation areas in the Northern and Southern Hemispheres were similar as it was near equinox when the solar flares occurred. As the TEC

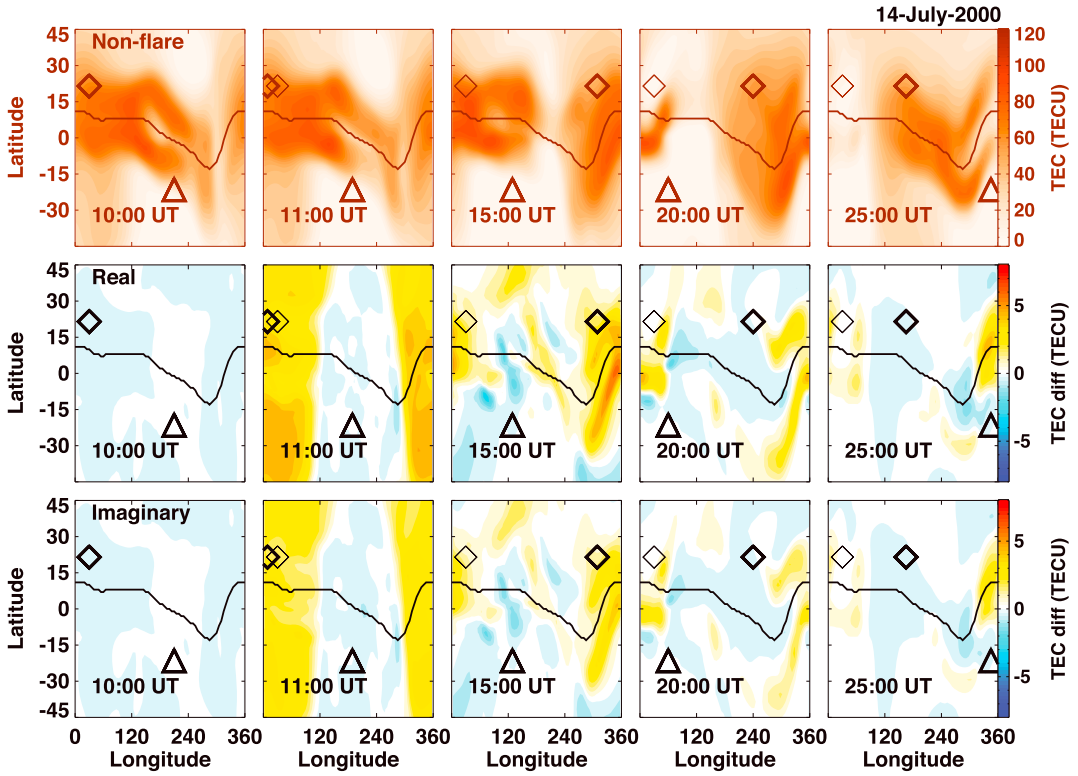

Figure 6. (top row) The midlatitude TEC of the nonflare simulation on 14–15 July 2000. (middle and bottom rows) The midlatitude TEC difference at the same time points. The diamonds and triangles mark the local noon and the local midnight respectively. The lighter diamond shows the subsolar point when the flare occurred. The line around 0° Latitude roughly presents the geomagnetic equator. The middle and bottom rows are for the real and the imaginary July flares, respectively.

returned to a background level, the perturbations were structured by the geomagnetic field. Two bands of high TEC existed at low latitudes, and bands with decreased TEC existed at midlatitudes at 2900 UT. These ionospheric structures were caused by the flare-induced neutral wind that flowed away from the flare subsolar region toward the high latitudes. The neutral wind pushed the two high bands away from the geomagnetic equator (as can be seen by the widening of the TEC enhancement bands from 2400 UT to 2900 UT) and pushed the ions farther down the field lines around ±30° latitude, resulting in bands of decreased TEC at middle latitudes.

In order to explore how long the ionospheric perturbation at the subsolar point lasted, the average ionospheric density in the region that was within 30° of the subsolar point at the time of the flare was plotted (i.e., the region around the light diamonds in Figure 6). Figure 8 shows plots of the electron density as a function of altitude and UT in this region above the Earth. Figure 8 (left) shows the difference in electron density for the July flare. Both the actual and imaginary flare irradiances caused ionization deep into the lower thermosphere with the peak enhancement occurring between 200 and 300 km altitude. The electron density perturbation below 300 km lasted for around 1 h, while the perturbation in the upper ionosphere lasted for approximately 21 h, which was long enough for that spot to rotate to the nightside and cause a perturbation in TEC. As mentioned above, the real July flare, with more energy, caused greater and longer perturbations.

Figure 8 (right) shows the average electron perturbation within 30° of the subsolar point when the April flare occurred (i.e., the region around the light diamonds in Figure 7). The imaginary April flare caused a larger electron perturbation as it contained more energy. However, the electron perturbations caused by the two flares lasted equally long (approximately 21 h). The slight increase in the density observed above 500 km around hours 24–25 in the imaginary flare may have resulted from the small secondary flare. In addition, the small electron perturbations during hours 0–12 were caused by the three small flares at the beginning of the day before. Examination of the background electron density shows that the structure of

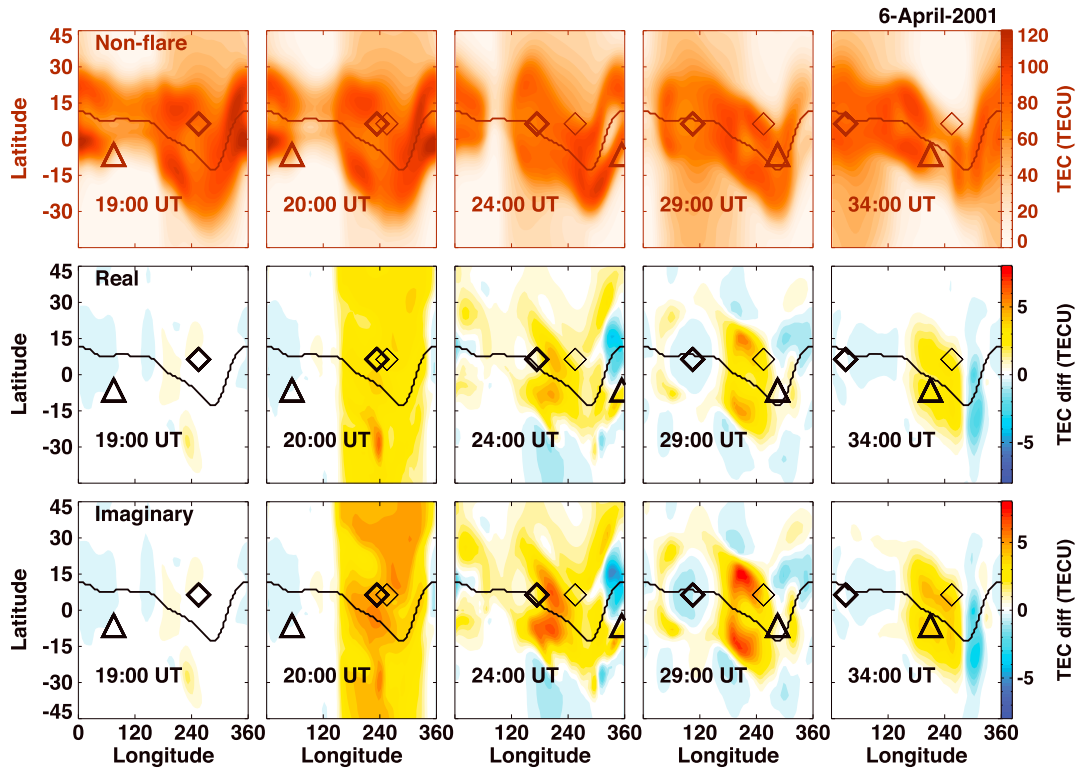

Figure 7. (top row) The midlatitude TEC of the nonflare simulation on 6–7 April 2001. (middle and bottom rows) The midlatitude TEC difference at the same time points. The diamonds and the triangles mark the local noon and the local midnight respectively. The lighter diamond shows the subsolar point when the flare occurred. The line around 0° Latitude roughly presents the geomagnetic equator. The middle and bottom rows are for the real and the imaginary April flares respectively.

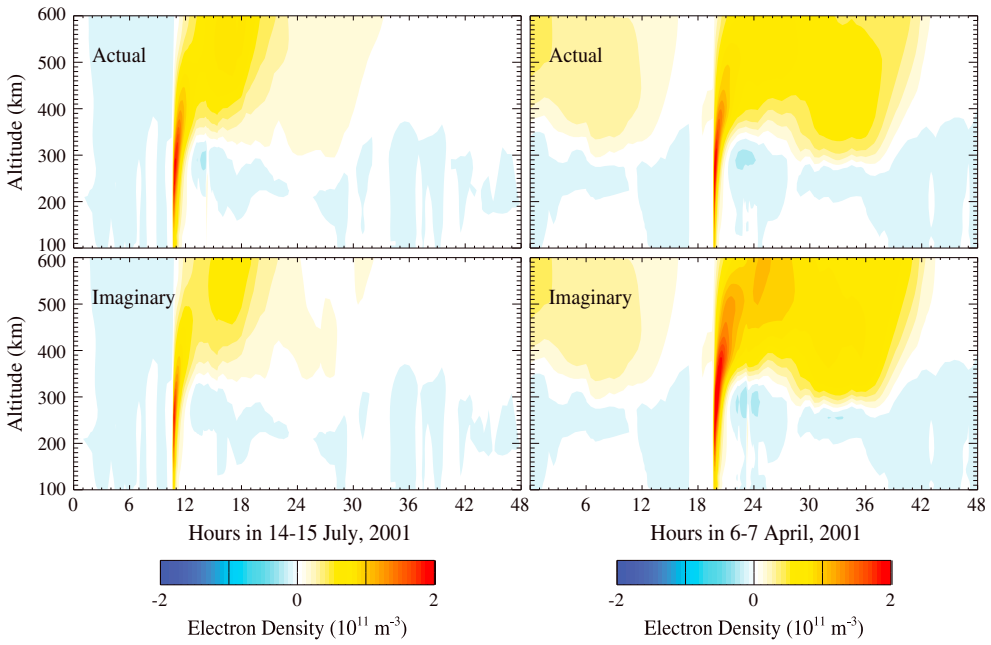

Figure 8. Average electron density difference within 30° SZA of a fixed site (subsolar at the flare time) (left) on 14–15 July 2000 and (right) on 4–6 April 2001. The top and bottom rows present the real and imaginary flare respectively.

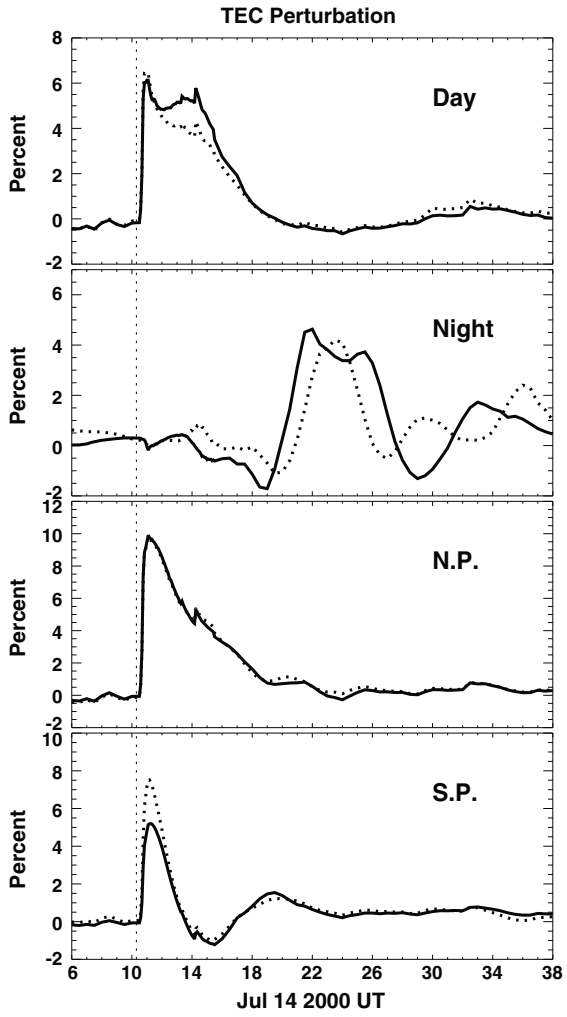

Figure 9. Regionally averaged TEC perturbation on 14–15 July 2000. Regions were defined the same as that in Figure 4. The solid line and the dashed line are for the real July flare with the realistic geomagnetic field (IGRF) and with an ideal dipole magnetic field respectively. The dashed vertical lines indicate the time that the flare onset.

the electron density perturbation is similar to the structure of the background electron density. The flares just added a small increment to the background structure.

4.2. Background Influence

When this study was started, there was an expectation that the ionospheric response to the real July flare and the imaginary April flare (i.e., July flare moved to April) would be similar and the ionospheric response to the real April flare and imaginary July flare (i.e., April flare moved to July) would be similar. In other words, it was expected that the solar irradiance spectrum would be the dominant controlling factor, while the response of the ionosphere between the real and imaginary flares during the same period would be different. This did not happen. The ionosphere reacted quite differently to the exact same flare spectrum in April versus July. Because of this, it was theorized that the background condition had a significant influence on the ionospheric reaction to the flare, while the spectrum had less of an influence. In order to test this, more simulations were conducted. Specifically, the magnetic field topology and season were altered in order to explore their influence. The topology was investigated because the two flares occurred when different magnetic geometries were facing the Sun, while the two flares took place in different seasons, so this was also investigated.

4.2.1. Geomagnetic Field

The real July flare was simulated again, this time using an ideal dipole field. Once again, two simulations were run, one with the 1 min FISM data and one with the 12 h median-filtered FISM data. These were differenced as before to calculate the perturbation TEC.

Figure 9 shows the comparison between the regionally averaged TEC perturbation caused by the real July flare with the IGRF and the July flare with the dipole magnetic field. The solid line represents the TEC perturbation with the realistic geomagnetic field (the same as Figure 4), while the dashed line shows the simulation with an ideal dipole magnetic field. Compared with IGRF, the run with the dipole field had a lower average TEC perturbation on the dayside and nightside, with an increased perturbation in the south polar region. In the north polar region, the response was almost identical.

On the dayside, the initial perturbation was almost identical, while the reaction 2–5 h after the flare differed by a small amount. This difference between the two simulations may have been caused by two mechanisms: first, the smoother topology of the ideal dipole field allowed neutral winds to drag ions more easily away from the dayside along field lines, which led to a more rapid decrease of the dayside TEC perturbation in the run with the ideal dipole field. Second, the change in field strength influenced the electrodynamics on the dayside, which affected the TEC response in this region. However, it was difficult to determine which factor was more important. The percent perturbation of the averaged TEC in the south polar region of the dipole case was higher than that in the IGRF case. This was because the baseline run with the smoothed FISM drivers and the dipole field had a lower average TEC in the south polar region than the baseline run with

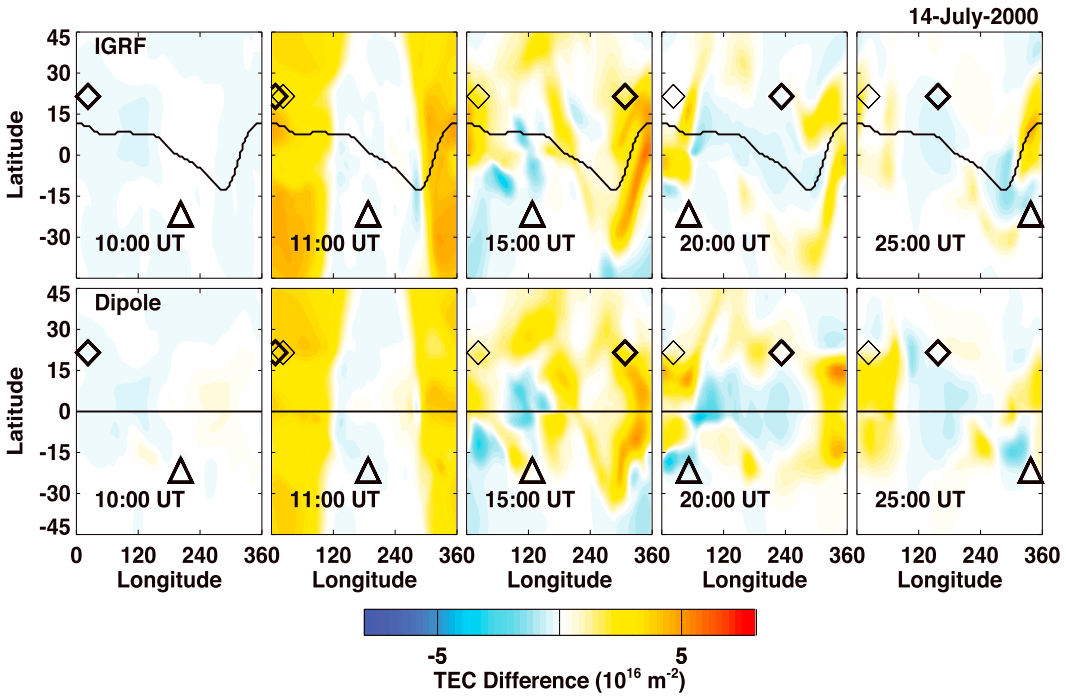

Figure 10. Midlatitude TEC difference on 14–15 July 2000. The diamonds and triangles mark the local noon and the local midnight respectively. The lighter diamond shows the subsolar point when the flare occurred. The line around 0° Latitude roughly presents the geomagnetic equator. (top row) The real July flare with the APEX; (bottom row) the real July flare with dipole field.

IGRF. This caused the percentage variation to be larger in dipole case even though the total perturbation was similar between the two cases.

The perturbations on the nightside showed more disagreement between the two cases. This was because it took 12 h for the perturbation to rotate to the nightside. During this time, background processes influenced by the structure of the magnetic field, such as the momentum coupling between the ions and neutrals, changed the evolution of the TEC perturbation. This is illustrated in Figure 10, which shows the distribution of the midlatitude TEC difference caused by the real July flare with IGRF (top row) and with the dipole field (bottom row). The magnitudes of the TEC perturbations were almost identical in the two cases, while the distribution of TEC in the two cases showed significant differences. The distribution of the IGRF TEC perturbation was along the curve of the magnetic equator, but because the dipole equator was the same as the geographic equator, the TEC perturbation in the dipole case was more symmetric around the geographic equator. The structure of the geomagnetic field was important in determining the postflare evolution of TEC distribution. As is shown at 2000 UT in Figure 10, the perturbation evolved differently as it rotated to the nightside. There are some interesting similarities too. For example, at 1500 UT, between 120 and 240 longitude, the perturbation in the north was stronger (although in a different shape). Between 240 and 360 longitude, the perturbation in the south was stronger, but the shape was different. This illustrates that the background wind pattern was similar, but the ion-neutral coupling was different due to the magnetic field topology.

The difference between simulations with and without IGRF was very small compared to the difference between the real July and the imaginary April flares as well as the real April and the imaginary April flares. This indicates that magnetic field structure probably has a large influence on the nightside reaction to the flare but less of an effect on the other regions.

4.2.2. Season

To explore the effect of different seasons on the ionospheric reaction to solar flares, the 13–15 July flare time period (including EUV, solar wind, IMF, and hemispheric power inputs) was shifted to 13–15 March. In other words, all the forcing of the July run and the March run were the same except that they were in different seasons. Figure 11 shows the regionally averaged TEC perturbations caused by the July flare (solid line) and

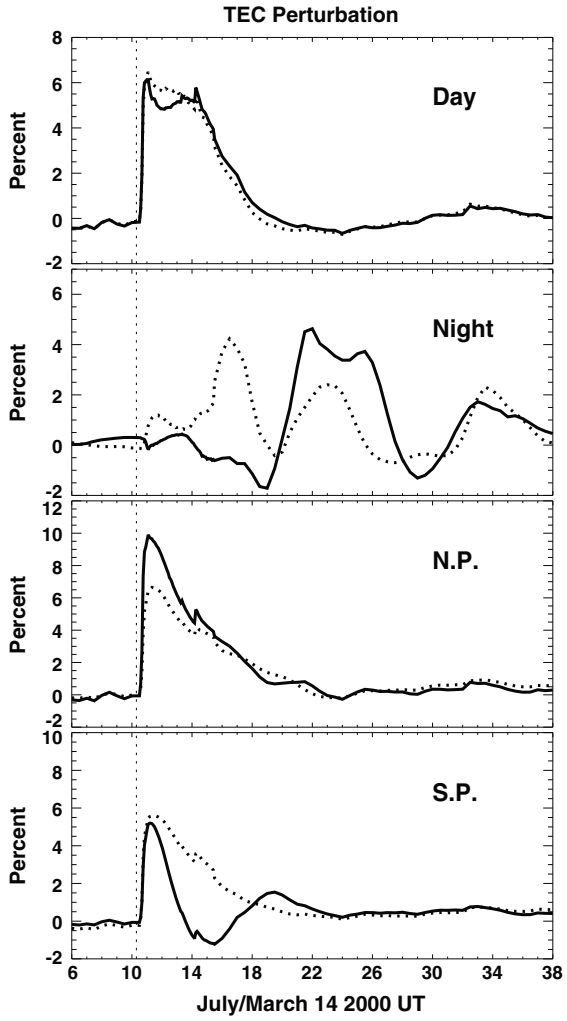

Figure 11. Regional average TEC perturbation on 14–15 July/March. The solid line and the dashed line are for the July and March flares respectively. The vertical dashed line indicates the time that the flare occurred.

the July flare moved to the March time (dashed line). The north polar TEC had a larger perturbation than the south polar TEC in the July case as it was summer in the Northern Hemisphere, while in the March case, the perturbations in the polar regions were similar because it was near the March equinox. The dayside was only slightly modified by the seasonal difference. The nightside response, however, was significantly different. Rather than a 12 h delay in the July case, the March nightside perturbation occurred about 5 h earlier.

Figure 12 shows the low and middle latitude distribution of the TEC difference caused by the July flare (top row) and the March flare (bottom row). The distribution of the perturbations in the two cases were similar on the dayside (at the diamonds). Although the March flare had a stronger absolute perturbation, as Figure 11 shows, the relative perturbations were nearly the same. During the March flare, there was a small perturbation on the nightside. Because this was so fast after the flare onset, the only mechanism that could have caused this response was a change in the equatorial electroject, which caused a small uplift in the *F* region on the nightside, reducing the loss rate, which appeared as a slight density increase in the difference plots. At 1500 UT, the nightside TEC perturbation (near the triangle) was more extensive in March than in July, as is indicated by the large perturbation a few hours after the flare in Figure 11. This appears to be primarily due to the fact that the anti-subsolar point was very close to the magnetic field equator during the March time but was far away from the equator during the July time. During July, the anti-subsolar point was about 21.5° away from the geomagnetic equator to the south, which led to downward ion flows around midnight. The solar flare intensified this downward flow and caused a decrease in TEC on the nightside, which is shown as the blue region (near the triangle) at 1500 UT. However, in March, the anti-subsolar point was almost right at the magnetic equator, which led to the converging neutral wind primarily pushing the ionosphere upward around midnight. The neutral wind was intensified by the solar flare, causing the TEC to increase on the nightside between 15 and 18 UT. As shown in Figure 13, the nightside perturbation in neutral density at 413 km and the perturbation in TEC were well matched in time, although the TEC perturbation reduced more rapidly than the neutral density perturbation.

4.3. Comparison With GPS

In order to determine whether the simulated response of the ionosphere to the solar flares was realistic, a comparison between the modeled TEC and measured TEC was conducted. Figure 14 shows the relationship between the TEC difference (simulation with the flare minus simulation without the flare) and the SZA at 1100 UT on 14 July 2000. There appears to be two linear relationships, one below 80° and one above 80°. The largest TEC enhancement of approximately 5 total electron content unit, 1 TECU = 10^{16} el m^{-2}, (TECU) existed at SZAs between 10°–15° and 30°–40°. At each solar zenith angle, there is a large spread

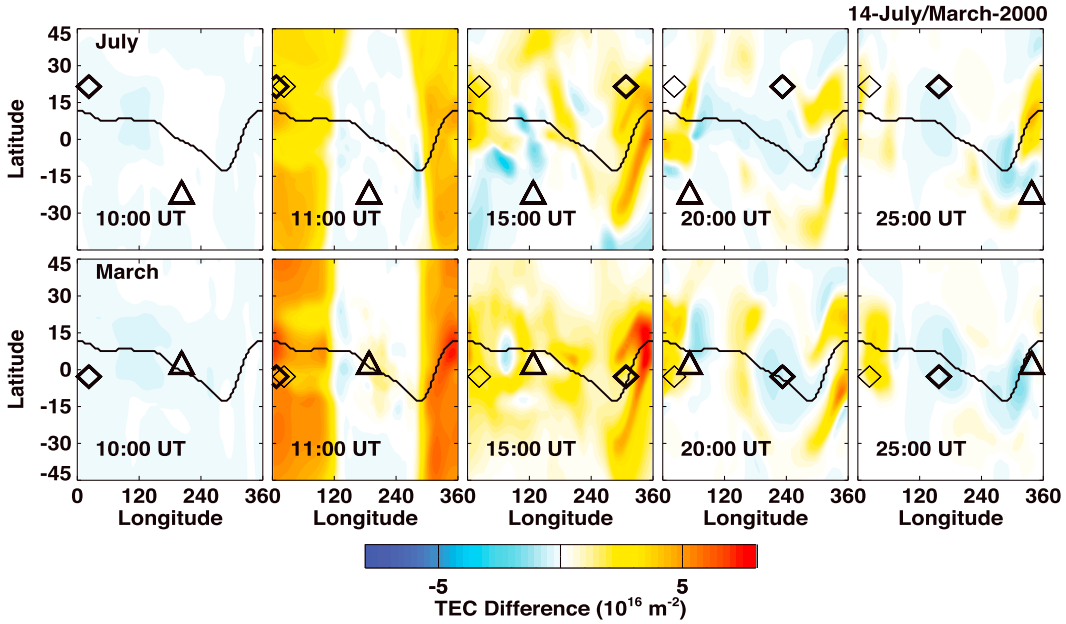

Figure 12. Midlatitude TEC difference on 14 July/March 2000. The diamonds and triangles mark the local noon and the local midnight respectively. The lighter diamond shows the subsolar point when the flare occurred. The line around 0° Latitude roughly presents the geomagnetic equator. (top and bottom rows) For the July and March flares respectively.

in the TEC, which is most likely due to the magnetic field topology causing different ion-neutral coupling processes at the same SZA but very different latitudes and longitudes. The similar plot of a comparison between TEC enhancements derived from TEC observations and their corresponding solar zenith angles during the same flare was present in *Zhang and Xiao* [2002]. The GPS TEC enhancements related to the enhancement in the solar irradiation due to the flare were derived from each temporal TEC curve by removing the influence of the background solar disk irradiation. Near the shadow boundary region with SZAs between 80° and 105°, TEC enhancement still existed but decreased rapidly with SZA. These findings agree with the GPS observations during the flare on 28 October 2003 obtained in *Zhang and Xiao* [2005].

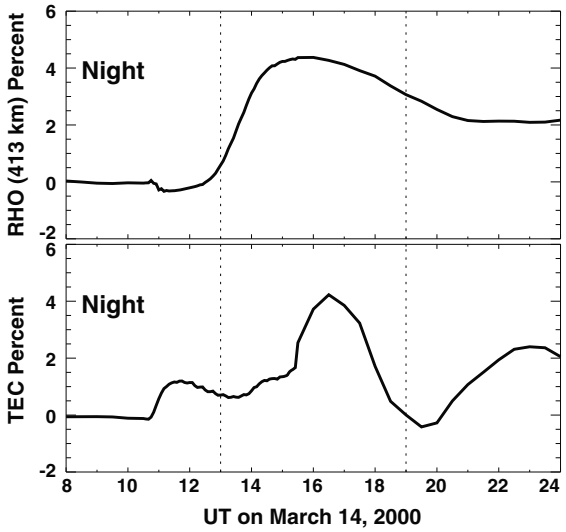

Figure 13. (top) Nightside neutral density perturbation at 413 km altitude and (bottom) nightside TEC perturbation on 14 March 2000.

Figure 15 shows the modeled (top and middle rows) and measured (bottom row) low-latitude and midlatitude TEC changes that took place during and after the flare in July 2000. The TEC changes here were derived by subtracting the TEC (model results and measurements) 30 min before from the TEC at the plotted time. The top row shows the TEC changes from 1000 UT to 2500 UT on 14 July 2000 in the same format as Figure 6, although the differencing method was different. At 1000 UT, small TEC enhancements occurred on the dayside and some regions around the equator on the nightside. At 1100 UT, large TEC enhancements occurred across the dayside and large TEC decreases occurred on the nightside. The narrow positive enhancement that extended across all latitudes in each plot is the morning terminator. The dusk terminator is more difficult to locate. At 1500 UT, the enhancement region on the dayside was moving westward with the subsolar point. From 1500 UT to 2500 UT the enhancement

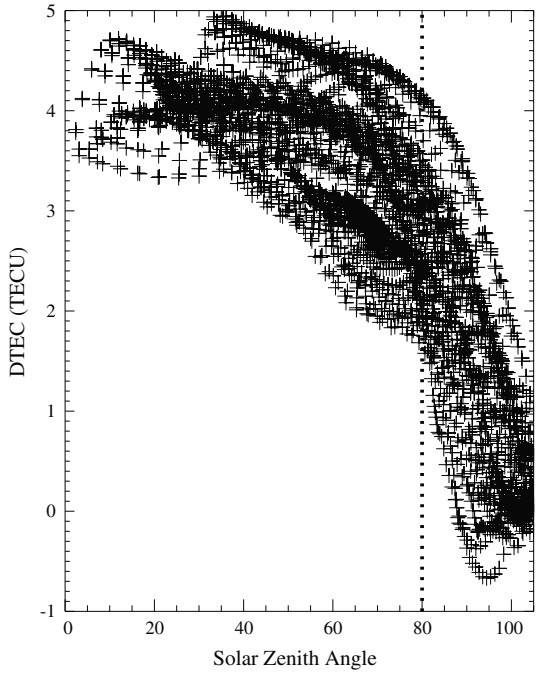

Figure 14. TEC difference versus the solar zenith angle on the dayside and the sunlit boundary region at 1100 UT on 14 July 2000. The vertical dashed line marks the SZA of 80°.

region on the dayside extended slightly in longitude. The middle and bottom rows show the TEC changes from the model and from the GPS observation at all the available GPS sites [*Madrigal*, 2014]. At 1000 UT, both the model and GPS showed large areas of negative changes except a small region near dawn. At 1100 UT, both the model and GPS showed the dayside TEC enhancements caused by the flare near the 300° longitude sector (i.e., the North and South American sector). The model also showed that the enhancement extended to 0°–120° longitude northward of the subsolar point, while the GPS showed decreased values in the same area. At 1500 UT, both model and observation showed enhancements near the dawn sector. The GPS measurements also show some increases near 100° longitude, while the model enhancements in these regions were not as large as those in the observations. At 2000 UT, an enhancement region occurred near 150° longitude in the Southern Hemisphere and a decrease occurred near −45° longitude in the Northern Hemisphere both in model and in the observations. At approximately 240° longitude in the model, a decrease was observed, while an enhancement was observed in the data. At 2500 UT, both the model and observation captured the TEC enhancement on the dayside from ~100° to ~240° and the depletions at night.

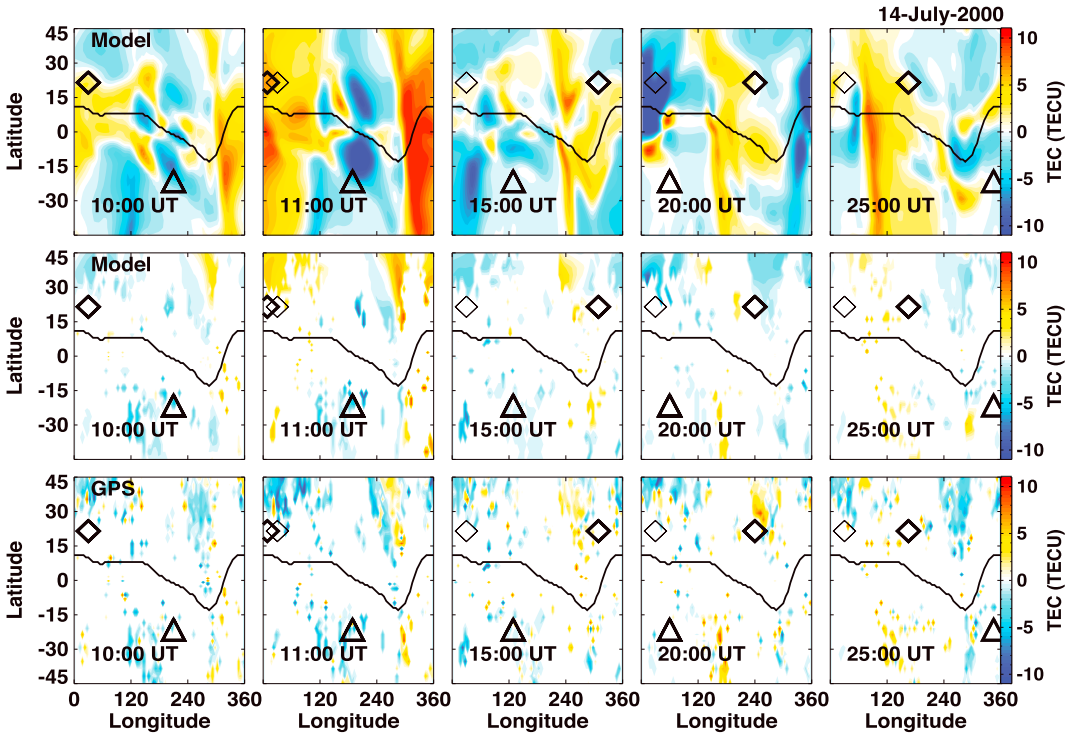

Figure 15. (top row) The TEC changes in model from 1000 UT to 2500 UT on 14 July 2000. (middle row) TEC changes in model (bottom row) by GPS at all available GPS sites at the same times as the top row.

5. Summary and Conclusions

In this study, the ionospheric perturbation caused by the two solar flares on 14 July 2000 and 6 April 2001 was examined with the global ionosphere and thermosphere model. Ideal experiments were conducted by exchanging the two flare spectra to produce imaginary solar flares. An unexpected result was that the ionospheric reactions to different flares with the same background conditions were very similar to each other, while moving the same flare to a different time caused the ionospheric reaction to be different. This indicates that the background conditions, as well as the total amount of energy in the flare (i.e., the strength and the duration of the flare), are two of the most important parameters in determining the ionospheric reaction to a flare. While the flare spectrum has been shown to be important [*Qian et al.*, 2010], this study indicates that the TEC perturbation is most sensitive to the background state and the total energy input during the flare. When different configurations of the magnetic field were explored, the differences were not very dramatic, leading to the conclusion that while the magnetic field topology is important, changing the topology does not appear to significantly alter the ionospheric reaction to the flare, except on the nightside. On the other hand, having the flare take place in a different season causes the reaction to the flare to be quite different everywhere but close to the subsolar point. In the polar regions, the perturbation is controlled by the tilt of the Earth, controlling how much flare irradiance enters the atmosphere in the given hemisphere. During equinox, the reactions in the Northern and Southern Hemispheres are almost identical, while the summer hemisphere has a stronger reaction than the winter hemisphere during solstice, as expected. On the nightside, the dynamics are much more complex, and the TEC appears to be controlled by the background winds. Having different wind patterns during different seasons changes the forcing of the ionosphere along field lines, which can dramatically alter the ionosphere over the 12 h that it takes the perturbation to rotate from the subsolar region to the midnight region. The simulations also show relatively good agreement with GPS observations, when the relationship between TEC enhancements due to the 14 July 2000 flare and local solar zenith angles were explored. The global maps of the TEC enhancements were generally in agreement between the simulation and GPS observations.

Acknowledgments

This work was partially supported by NASA grant NNX09AJ59G. We also are deeply indebted to P. Chamberlin for the FISM output that drove GITM for these flare events. Further, GITM utilized the ACE magnetometer, and SWEPAM measurements as well as the National Oceanic and Atmospheric Administration (NOAA) provided hemispheric power index to drive the high latitudes for these events.

Alan Rodger thanks L.A. Leonovich and an anonymous reviewer for their assistance in evaluating this paper.

References

Chamberlin, P. C., T. N. Woods, and F. G. Eparvier (2007), Flare irradiance spectral model (FISM): Daily component algorithms and results, *Space Weather*, *5*, S07005, doi:10.1029/2007SW000316.

Coster, A., and A. Komjathy (2008), Space weather and the Global Positioning System, *Space Weather*, *6*, S06D04, doi:10.1029/2008SW000400.

Davides, K. (1990), *Ionospheric Radio*, Peter Peregrinus Ltd., London, U. K.

Donnelly, R. F. (1967), The solar flare radiations responsible for sudden frequency deviations, *J. Geophys. Res.*, *101*, 5247–5256, doi:10.1029/95JA03676.

Fuller-Rowell, T., and D. Evans (1987), Height-integrated Pedersen and Hall conductivity patterns inferred from TIROS–NOAA satellite data, *J. Geophys. Res.*, *92*, 7606–7618.

Garriott, O. K., A. V. da Rosa, M. J. Davis, and J. O. G. Villard (1967), Solar flare effects in the ionosphere, *J. Geophys. Res.*, *72*, 6099–6103, doi:10.1029/JZ072i023p06099.

Hedin, A. (1987), MSIS-86 thermospheric model, *J. Geophys. Res.*, *92*, 4649–4662.

Huffman, R. E. (1969), Absorption cross-sections of atmospheric gases for use in aeronomy, *Can. J. Chem.*, *47*, 1823–1834, doi:10.1139/v69-298.

Jones, T. B. (1971), VLF phase anomalies due to a solar X-ray flare, *J. Atmos. Sol. Terr. Phys.*, *33*, 963–965.

Leonovich, L. A., E. L. Afraimovich, E. B. Romanova, and A. V. Taschilin (2002), Estimating the contribution from different ionospheric regions to the TEC response to the solar flares using data from the international GPS network, *Ann. Geophys.*, *20*, 1935–1941.

Leonovich, L. A., A. V. Tashchilin, and O. Y. Portnyagina (2010), Dependence of the ionospheric response on the solar flare parameters based on the theoretical modeling and GPS data, *Geomag. Aeron.*, *50*, 201–210, doi:10.1134/S0016793210020076.

Madrigal (2014), The open madrigal initiative. [Available at http://www.openmadrigal.org/.]

Mendillo, M., et al. (1974), Behavior of the ionospheric F region during the great solar flare of August 7, 1972, *J. Geophys. Res.*, *79*, 665–672, doi:10.1029/JA079i004p00665.

Pawlowski, D., and A. Ridley (2009), Modeling the ionospheric response to the 28 October 2003 solar flare due to coupling with the thermosphere, *Radio Sci.*, *44*, RS0A23, doi:10.1029/2008RS004081.

Pawlowski, D. J., and A. J. Ridley (2008), Modeling the thermospheric response to solar flares, *J. Geophys. Res.*, *113*, A10309, doi:10.1029/2008JA013182.

Qian, L., A. Burns, P. Chamberlin, and S. Solomon (2010), Flare location on the solar disk: Modeling the thermosphere and ionosphere response, *J. Geophys. Res.*, *115*, A09311, doi:10.1029/2009JA015225.

Qian, L., A. G. Burns, S. C. Solomon, and P. C. Chamberlin (2012), Solar flare impacts on ionospheric electrodynamics, *Geophys. Res. Lett.*, *39*, L06101, doi:10.1029/2012GL051102.

Richmond, A. D. (1995), Ionospheric electrodynamics using magnetic apex coordinates, *J. Geomagn. Geoelec.*, *47*, 191–212.

Rideout, W., and A. Coster (2006), Automated GPS processing for global total electron content data, *GPS Solut.*, *10*, 219–228, doi:10.1007/s10291-006-0029-5.

Ridley, A., Y. Deng, and G. Tòth (2006), The global ionosphere-thermosphere model, *J. Atmos. Sol. Terr. Phys.*, *68*, 839–864, doi:10.1016/j.jastp.2006.01.008.

SpaceWeatherLive (2014), Real-time auroral activity and solar activity. [Available at http://www.spaceweatherlive.com/en/solar-activity/.]

Stonehocker, G. H. (1970), Advanced telecommunication forecasting technique, in *Ionospheric Forecasting, AGARD CONF. Proc. No. 49, Advisory Group for Aerospace Research and Development*, edited by V. Agy, pp. 27–31, NATO, Brussels, Belgium.

SWPC (2013), Historical SWP products from 1996. [Available at http://www.swpc.noaa.gov/ftpmenu/warehouse.html/.]

Tsurutani, B. T., O. Verkhoglyadova, A. J. Mannucci, G. S. Lakhina, G. Li, and G. P. Zan (2009), A brief review of "solar flare effects" on the ionosphere, *Radio Sci.*, *44*, RS0A17, doi:10.1029/2008RS004029.

Tsurutani, B. T., et al. (2005), The Octorber 28, 2003 extreme EUV solar flare and resultant extreme ionospheric effects: Comparison to other halloween events and the bastille day event, *Geophys. Res. Lett.*, *32*, L03S09, doi:10.1029/2004GL021475.

Wan, W., L. Liu, H. Yuan, B. Ning, and S. Zhang (2005), The GPS measured SITEC caused by the very intense solar flare on July 14, 2000, *Adv. Space Res.*, *36*, 2465–2469.

Weimer, D. R. (2005), Improved ionospheric electrodynamic models and application to calculating Joule heating rates, *J. Geophys. Res.*, *110*, A05306, doi:10.1029/2004JA010884.

Worden, J. R., T. N. Woods, and K. W. Bowman (2010), Far-ultraviolet intensities and center-to-limb variations of active regions and quiet sun using UARS SOLSTICE irradiance measurements and ground-based spectroheliograms, *Astrophys. J.*, *560*, 1020, doi:10.1086/323058.

Xiong, B., W. Wan, B. Ning, F. Ding, L. Hu, and Y. Yu (2013), A statistic study of ionospheric solar flare activity indicator, *Space Weather*, *12*, 29–40, doi:10.1002/2013SW001000.

Xiong, B., et al. (2011), Ionospheric response to the X-class solar flare on 7 September 2005, *J. Geophys. Res.*, *116*, A11317, doi:10.1029/2011JA016961.

Zhang, D., and Z. Xiao (2003), Study of the ionospheric total electron content response to the great flare on 15 April 2001 using international GPS service network for the whole sunlit hemisphere, *J. Geophys. Res.*, *108*(A8), 1330, doi:10.1029/2002JA009822.

Zhang, D., and Z. Xiao (2005), Study of ionospheric response to the 4b flare on 28 October 2003 using internation GPS service network data, *J. Geophys. Res*, *110*, A03307, doi:10.1029/2004JA010738.

Zhang, D. H., and Z. Xiao (2002), GPS-derived ionospheric total electron content response to a solar flare that occurred on 14 July 2000, *Radio Sci.*, *37*(5), 1086, doi:10.1029/2001RS002542.